PAPER

Check for updates

π−π stacking assisted regioselectivity regulation in palladium-catalyzed cyclization reactions: a theoretical study†

Song Liu, [ID] *[ab] Dianmin Zhang,*[a] Yue Gong,[a] Lianli Ma,[a] Li Li[a] and Wei Chen[a]

The regulation of regioselectivity is an objective often pursued by organic chemists, and the comprehension of its mechanisms is crucial for devising efficient synthetic pathways. In this report, we conducted theoretical calculations to explore the regioselectivity regulatory mechanisms of two palladium-catalyzed cyclization reactions. In these cyclization reactions, manipulating the structural differences in the reaction substrates leads to the formation of distinct products. A detailed reaction mechanism and reactivity profile for this reaction were revealed. Furthermore, a π−π stacking assisted regioselectivity regulatory mechanism was proven by distortion−interaction energy analysis and noncovalent interaction calculations. The calculated results presented herein provide a theoretical guide for further experimental investigations of regioselectivity regulation.

Introduction

Regioselectivity is an important field in organic synthetic chemistry that mainly focuses on the differences in reactivity at various positions on a substrate.[1] Several reactive sites may exhibit similar activity, leading to the formation of a mixture of isomers in the final product. Catalytic methods are ideal synthetic approaches in organic chemistry, as they allow for the prediction and switching of regioselectivity to access site-diverse regioisomers by altering the fewest reaction parameters.[2]

Various regulatory strategies in organic chemistry, such as steric effects,[3] electronic effects,[4] chelation control,[5] and ligand control,[6] have been used to achieve regioselectivity[7] (Scheme 1a). Chemists can use these strategies to manipulate the outcome of organic reactions to achieve certain modifications at specific sites within complex molecules, but the regulatory mechanism of regioselectivity is often ambiguous. In organic synthesis, understanding the regulatory mechanisms of these strategies is essential for designing efficient synthetic routes to obtain the targeted products.[8]

Recently, Huang *et al.* described two palladium (Pd)-catalyzed cyclization reactions of enynols with aminals.[9] In their reports, different products were obtained by manipulating the skeletal variances of substrates. As shown in Scheme 1b, the

use of (2-(but-3-en-1-yn-1-yl)phenyl)methanol as the substrate led to the predominant formation of the *O*-heterocycle-containing allenic amine product **4**. Furthermore, the use of hept-6-en-4-yn-1-ol as the substrate resulted in the formation of polysubstituted 1,3-diene embedded in *O*-heterocycle **5** as the main product (Scheme 1b). Control experiments confirmed the non-cyclic allenic 1,5-diamine **3** as the key intermediate in both cyclization reactions. However, the detailed regioselectivity
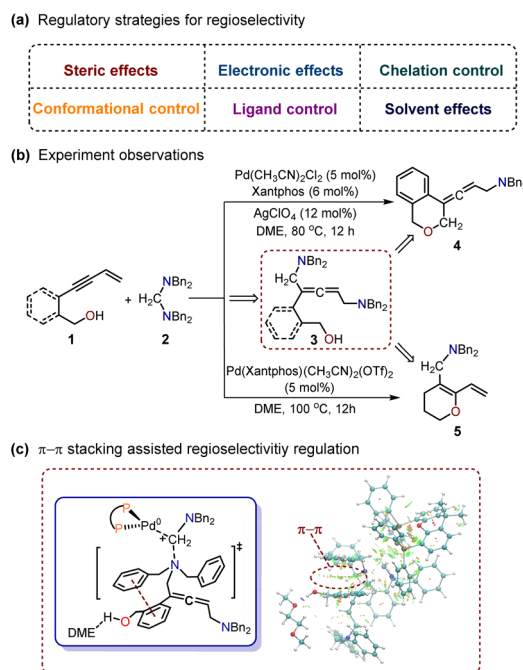
Scheme 1 Palladium-catalyzed cyclization of enynols with aminals.

[a]Chongqing Key Laboratory for Resource Utilization of Heavy Metal Wastewater, College of Chemistry and Environmental Engineering, Chongqing University of Arts and Sciences, Yongchuan, 402160, PR China. E-mail: sliu@cqwu.edu.cn

[b]School of Chemistry and Chemical Engineering, Chongqing University, Chongqing, 400030, China

regulatory mechanism for these Pd-catalyzed cyclizations is still not clear. Herein, we used density functional theory (DFT) calculations to explore these Pd-catalyzed cyclization reactions and proposed a π–π stacking assisted regioselectivity regulatory mechanism (Scheme 1c). A detailed reaction mechanism and reactivity profile were also provided.

Computational methods

All DFT calculations were carried out with Gaussian 16.[10] The B3LYP functional[11] with a standard 6-31G(d) basis set (the SDD basis set for Pd) was used for geometry optimizations. Harmonic frequency calculations were performed for all stationary points to confirm them as local minima or transition structures and to derive the thermochemical corrections of the enthalpies and free energies. All minima had zero imaginary frequency and all transition states had only one imaginary frequency. The solvent effects were considered by single-point calculations on the gas-phase stationary points with the SMD continuum solvation model.[12] The M06 (ref. 13) functional with the 6-311+g(d) basis set (the SDD basis set for Pd) was used to calculate the single-point energies with dimethyl ether as the solvent. For the 1,2-dimethoxyethane (DME) solvent data not included in Gaussian 16, the key parameters were set in the input file manually (for 1,2-dimethoxyethane, eps = 7.2, while the other parameters were the same as those for diethyl ether). The energies given in this report were the M06 calculated Gibbs free energies in 1,2-dimethoxyethane solvent. The optimized structures were displayed using CYLview.[14] The distortion and interaction energies were calculated B3LYP functional with the 6-31G(d) basis set. Additionally, a basis set superposition error (BSSE)[15] correction was applied when calculating the interaction energies. The noncovalent interactions (NCIs)[16] were calculated using B3LYP-D3 functional with the 6-31G(d) basis set.

The global reactivity index values were also calculated using the M06 functional and the 6-311+g(d) basis set for all atoms. The N (global nucleophilicity index)[17] values were calculated with eqn (1), where ε_{HOMO} refers to the orbital energy of the highest occupied molecular orbital (HOMO) and ε_{LOMO} refers to the orbital energy of the lowest unoccupied molecular orbital (LUMO). In eqn (1), tetracyanoethylene (TCE) with the lowest HOMO energy among the organic molecules was used as a ref. 18.
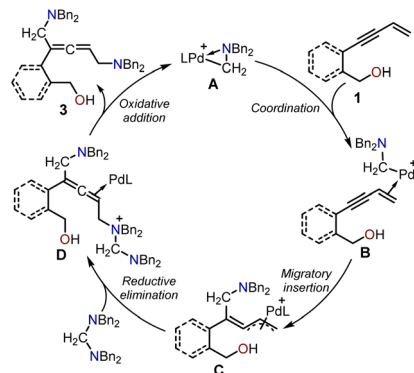
$$N = \varepsilon_{HOMO} \text{ (Nu)} - \varepsilon_{HOMO} \text{ (TCE)} \qquad (1)$$

The N_k (local nucleophilicity index) values were calculated according to eqn (2), where the f_k^- (condensed Fukui function) values can be obtained by $f_k^- = q_k(N-1) - q_k(N)$.[19]

$$N_k = N \times f_k^- \qquad (2)$$

Results and discussion

The proposed catalytic cycle for the Pd-catalyzed cyclization of enynols with aminals is illustrated in Schemes 2 and 3. Scheme

Scheme 2 The proposed catalytic cycle for the production of intermediate **3**.

2 depicts the catalytic cycle for the allenic 1,5-diamine intermediate **3**. The aminomethyl cyclopalladated complex **A** was the active catalyst in both cyclizations. The coordination of the terminal alkene in the enynol substrate **1** with the Pd(II) center generated intermediate **B**. The subsequent migratory insertion of the enyne triple bond into the Pd(II)–C bond provided the π-allylpalladium intermediate **C**, which was intercepted by an aminal to form intermediate **D** *via* an S$_N$2-type reductive elimination process. Finally, the S$_N$2-type oxidative addition of the amino cation to the Pd(0) center afforded the non-cyclic allenic 1,5-diamine intermediate **3** together and regenerated the active Pd complex **A** to complete the catalytic cycle.

The proposed catalytic cycles in the production of the allenic amine **4** and the 1,3-diene *O*-heterocycle product **5** are depicted in Scheme 3. By employing (2-(but-3-en-1-yn-1-yl)phenyl) methanol **1** as the substrate in Path I, the ^{1}N atom in intermediate **3** can serve as a nucleophilic site to interact with the cyclopalladated complex **A** through S$_N$2-type reductive elimination, resulting in the formation of the quaternary ammonium intermediate **E** and Pd(0). The intermediate **E** is intramolecularly intercepted by the pendent alcohol through S$_N$2-type substitution to yield the desired product **4**. Finally, the S$_N$2-type
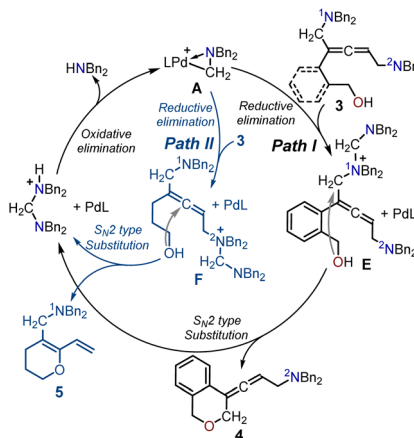
Scheme 3 Proposed catalytic cycle for the generation of the allenic amine product **4** and 1,3-diene *O*-heterocycle **5**.

oxidative addition of the generated amino cation to the Pd(0) center regenerated the active palladium-complex **A** to complete the catalytic cycle. Moreover, the use of hept-6-en-4-yn-1-ol **1′** as the substrate led to the ²N atom in intermediate **3** acting as a nucleophilic site to attack the Pd complex **A**, forming the quaternary ammonium intermediate **F**. The allene in intermediate **F** was intercepted by the pendent alcohol to give the 1,3-diene *O*-heterocycle product **5**.

The calculated free energy profiles for the generation of intermediate **3** using (2-(but-3-en-1-yn-1-yl)phenyl)methanol **1** as the substrate are presented in Fig. 1, with the aminomethyl cyclopalladated complex **INT1** serving as the reference zero point. The binding of the terminal alkene in the enynol substrate **1** to the Pd(ıı) center led to the endergonic generation of intermediate **INT2** (12.9 kcal mol⁻¹). The subsequent migratory insertion of the enyne triple bond into the Pd(ıı)–C bond took place through the transition state **TS1**, resulting in the formation of the π-allylpalladium intermediate **INT3**, with a free energy barrier of 12.2 kcal mol⁻¹. In transition state **TS1**, the length of the formed C–C bond is 2.19 Å. The intermediate **INT3** would then be intercepted by an aminal, leading to the formation of allene-coordinated Pd(0) intermediate **INT4** through an S$_N$2-type reductive elimination transition state **TS2** (activation free energy = 27.0 kcal mol⁻¹). In the transition state **TS2**, the length of the formed C–N bond is 1.97 Å. The following S$_N$2-type oxidative addition occurred between Pd(0) and the amino cation *via* transition state **TS3**, with an energy barrier of 4.4 kcal mol⁻¹. The release of the allenic 1,5-diamine intermediate **3** led to the exothermic formation of the aminomethyl cyclopalladated complex **INT1** (4.3 kcal mol⁻¹) in comparison with substrates **1** and **2**. Moreover, the calculated free energy profiles for the generation of intermediate **3′** using hept-6-en-4-yn-1-ol **1′** as the substrate are presented in Fig. S1.†
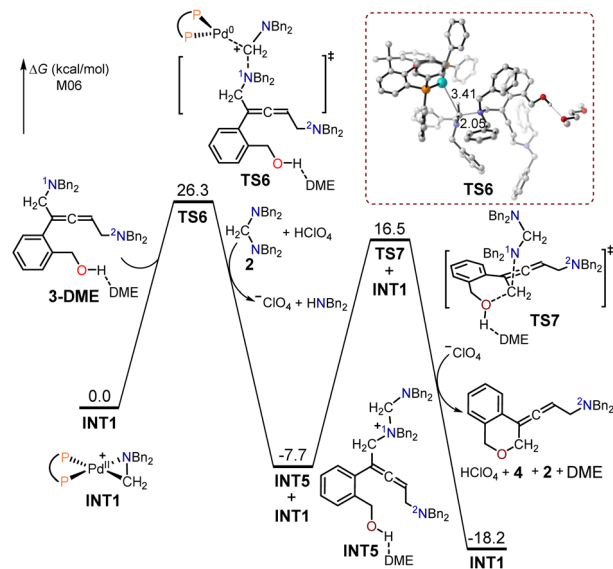

Fig. 2 Calculated free energy profiles for the production of the allenic amine product **4** using (2-(but-3-en-1-yn-1-yl)phenyl)methanol **1** as the substrate.

The π-allylpalladium in **INT3** can be intercepted by the tethered alcohol to form the 1,3-diene *O*-heterocycle product **5** through the S$_N$2-type reductive elimination transition states **TS4** and **TS5**. In **TS4**, the aminal substrate functioned as a base to facilitate reductive elimination, while the intramolecular amido group in transition state **TS5** assisted in reductive elimination. The energies of **TS4** and **TS5** were respectively 1.1 and 21.6 kcal mol⁻¹ higher than that of **TS2**, indicating that these pathways were unfavorable.
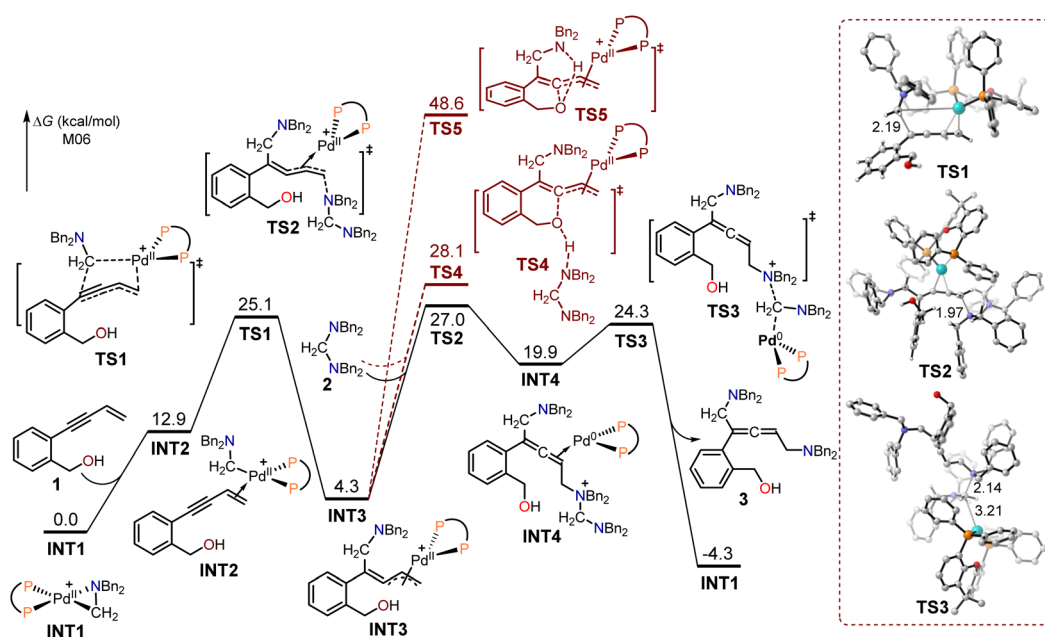

Fig. 1 Calculated free energy profiles for the production of intermediate **3** using (2-(but-3-en-1-yn-1-yl)phenyl)methanol **1** as the substrate.

The free energy profiles for the generation of the allenic amine product **4**, using (2-(but-3-en-1-yn-1-yl)phenyl)methanol **1** as the substrate are presented in Fig. 2. To investigate the effect of solvation on the system's structure and energy, an explicit DME molecule was included with substrate **3** to allow for the possibility of intermolecular hydrogen bonding between the hydroxyl group of **3** and a solvent oxygen atom. In the absence of the solvent molecule, an artefactual and misleading intramolecular O–H⋯π hydrogen bond would occur. The ^{1}N atom in intermediate **3-DME** served as a nucleophilic site to interact with the cyclopalladated complex **INT1** through S_N2-type reductive elimination to provide the quaternary ammonium intermediate **INT5** and Pd(0). The free energy barrier for this S_N2-type reductive elimination transition state **TS6** is 26.3 kcal mol^{-1}; the formed C–N bond and broken C–Pd bond had lengths of 2.05 and 3.41 Å, respectively. The resulting Pd(0) was captured by the amino cation, produced through the protonation of the aminal with HClO$_4$, to form the cyclopalladated complex, **INT1**. The generated intermediate **INT5** was then intramolecularly intercepted by the pendent alcohol through the S_N2-type substitution transition state **TS7** with a free energy barrier of 24.2 kcal mol^{-1}, to yield the desired allenic amine product **4**.

The free energy profiles for the formation of the 1,3-diene *O*-heterocycle product **5′** using (2-(but-3-en-1-yn-1-yl)phenyl) methanol **1** as the substrate are depicted in Fig. 3. The ^{2}N atom in intermediate **3-DME** acted as a nucleophilic site to undergo S_N2-type reductive elimination with the cyclopalladated complex **INT1** to generate the quaternary ammonium intermediate **INT6**. The free energy barrier for the S_N2-type reductive elimination transition state **TS8** (28.8 kcal mol^{-1}) was 2.5 kcal mol^{-1} higher than that of **TS6**, as the use of (2-(but-3-en-1-yn-1-yl)phenyl)methanol as the substrate primary resulted in the formation of the allenic amine product **4**. In **TS8**, the

formed C–N bond had a length of 2.13 Å, while the broken C–Pd bond was 3.26 Å. The intermediate **INT6** is expected to undergo an intramolecular interception by the pendant alcohol through an S_N2-type substitution transition state **TS9**, resulting in the formation of the 1,3-diene *O*-heterocycle product **5′**.

The free energy profiles for the formation of the allenic amine product **4′** using hept-6-en-4-yn-1-ol **1′** as the substrate are depicted in Fig. 4. The ^{1}N atom in intermediate **3′-DME** functioned as a nucleophilic site that interacted with the cyclopalladated complex **INT1** *via* S_N2-type reductive elimination to create the quaternary ammonium intermediate **INT5′** and Pd(0). The energy barrier for this S_N2-type reductive elimination transition state **TS6′** was 33.1 kcal mol^{-1}. The resulting intermediate **INT5′** was further reacted intramolecularly with the adjacent alcohol *via* an S_N2-type substitution transition state **TS7′**, with a free energy barrier of 27.7 kcal mol^{-1}, to yield the allenic amine product **4′**.

The free energy profiles for the synthesis of the 1,3-diene *O*-heterocycle product **5** from the hept-6-en-4-yn-1-ol **1′** substrate are displayed in Fig. 5. The nitrogen atom (^{2}N) in intermediate **3′-DME** functioned as a nucleophilic site to undergo S_N2-type reductive elimination with the cyclopalladated complex **INT1**, producing the quaternary ammonium intermediate **INT6′**. The energy barrier for the S_N2-type reductive elimination transition state **TS8′** was 31.8 kcal mol^{-1}. The intermediate **INT6′** underwent intramolecular interception by the adjacent alcohol through an S_N2-type substitution transition state **TS9′**, with a free energy barrier of 29.9 kcal mol^{-1}, to yield the 1,3-diene *O*-heterocycle product **5**. **TS8′** had a free energy 1.3 kcal mol^{-1} lower than that of **TS6′**, and the free energy of the 1,3-diene *O*-heterocycle product **5** was 12.4 kcal mol^{-1} lower than that of the allenic amine product **4′**. These findings elucidate that the primary product formed was the 1,3-diene *O*-heterocycle product **5** when using hept-6-en-4-yn-1-ol as the substrate.
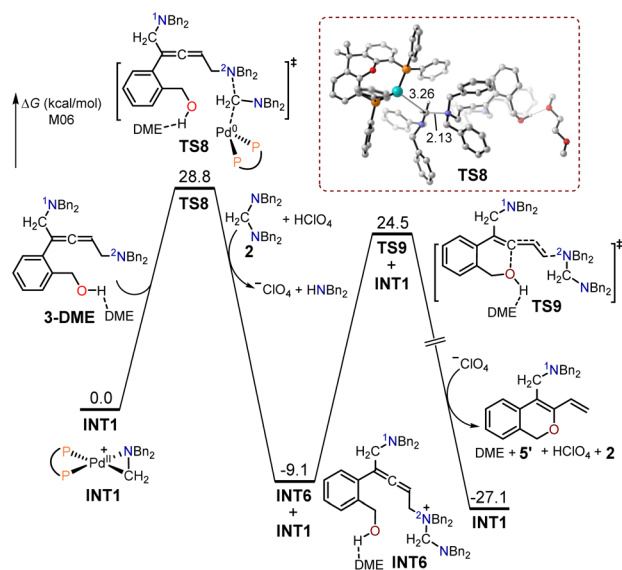

Fig. 3 Calculated free energy profiles for the production of the 1,3-diene *O*-heterocycle product **5′** using (2-(but-3-en-1-yn-1-yl)phenyl) methanol **1** as the substrate.
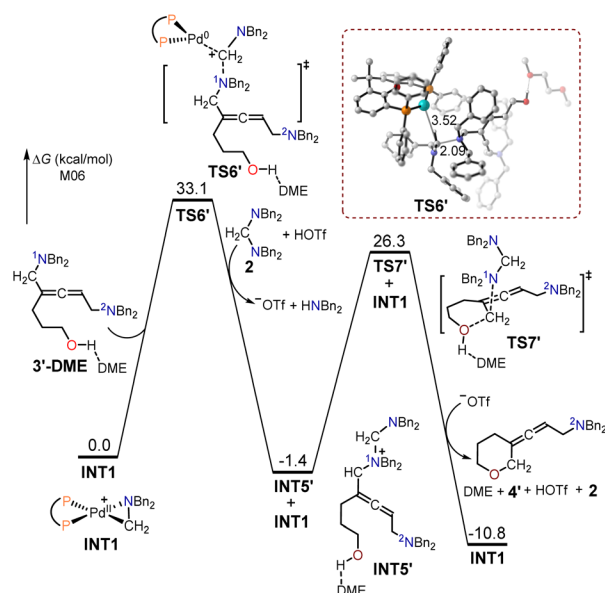

Fig. 4 Calculated free energy profiles for the production of the allenic amine product **4′** using hept-6-en-4-yn-1-ol **1′** as the substrate.
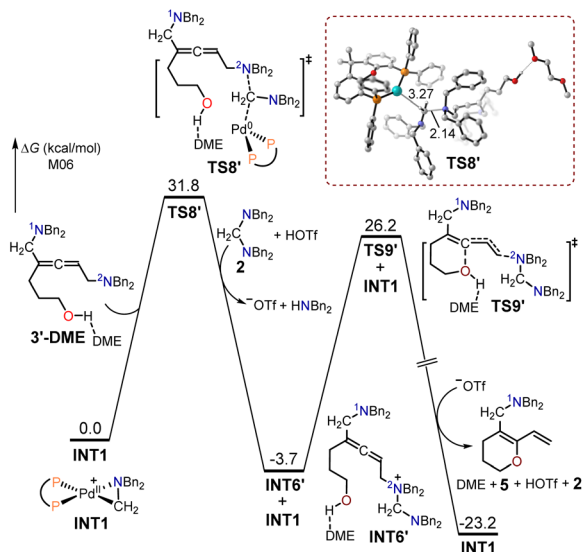
Fig. 5 Calculated free energy profiles for the production of the 1,3-diene O-heterocycle product 5 using hept-6-en-4-yn-1-ol 1′ as the substrate.

Table 1 Distortion and interaction energies of the transition states TS6 and TS6′. Values are given in kcal mol^{-1} ($\Delta E_{dist}^{\ddagger}$ is the distortion energies. $\Delta E_{int}^{\ddagger}$ is the interaction energies. $\Delta E^{\ddagger}$ is the reaction energies)

	$\Delta E_{dist(3\text{-}DME \text{ or } 3'\text{-}DME)}^{\ddagger}$	$\Delta E_{dist(INT1)}^{\ddagger}$	$\Delta E_{dist}^{\ddagger}$	$\Delta E_{int}^{\ddagger}$	$\Delta E^{\ddagger}$
TS6	9.5	35.9	45.4	−15.9	29.5
TS6′	11.2	37.2	48.4	−16.5	32.0

Distortion–interaction energy analysis was used to elucidate the disparity in the free energy barrier between transition states TS6 and TS6′. The distortion energy of TS6′ was 3.0 kcal mol^{-1} higher than that of TS6, while their interaction energies were similar (Table 1). The distortion energies of intermediates 3-DME and 3′-DME in TS6 and TS6′ were 9.5 and 11.2 kcal mol^{-1}, respectively. The distortion energy of INT1 in both TS6 and TS6′ were similar. Analysis of the distortion energy revealed that the difference in energy barriers of TS6 and TS6′ was controlled by the distortion energies of intermediates 3-DME and 3′-DME.

The structural information for intermediate 3-DME and transition state TS6 are shown in Fig. 7. In the optimized structure of intermediate 3-DME, the dihedral angle of ^{1}C–^{1}N–^{2}C–^{3}C is 95.7°, whereas this dihedral angle changes to 54.7° in TS6. In the optimized structure of intermediate 3′-DME, the dihedral angle of ^{1}C–^{1}N–^{2}C–^{3}C is −64.8°, which changes to 55.2° in TS6′ (Fig. 8). These calculated results indicated that the difference in free energy barrier between TS6 and TS6′ was controlled by the distortion of the benzyl group associated with ^{1}N in intermediates 3-DME and 3′-DME.

To further investigate the regioselectivity regulatory mechanism behind these Pd-catalyzed cyclization reactions, NCI analysis was conducted for transition states TS6 and TS6′. The π–π stacking of two phenyl rings in transition state TS6 occurred when (2-(but-3-en-1-yn-1-yl)phenyl)methanol 1 was used as the substrate (Fig. 9). By contrast, in transition state TS6′, there is solely a C–H···π interaction between the alkyl chain and phenyl group. NCI calculations revealed that the π–π stacking in TS6 are stronger than the C–H···π interactions in

The free energy barrier for TS6 was 6.8 kcal mol^{-1} lower than that of TS6′, whereas the free energy barriers for TS8 was 3.0 kcal mol^{-1} lower than that of TS8′. The reactivity of the ^{1}N atom decreased when the substrate was changed from (2-(but-3-en-1-yn-1-yl)phenyl)methanol 1 to hept-6-en-4-yn-1-ol 1′, whereas the reactivity of the ^{2}N atom remained unchanged. This difference in the reactivities of ^{1}N and ^{2}N contributed to the varying selectivity observed with different substrates.

The local nucleophilicity index N_k values were calculated to analyze the nucleophilicity of the nitrogen atoms (^{1}N and ^{2}N) in intermediates 3 and 3′. The calculated N_k values for ^{1}N and ^{2}N in intermediate 3 were respectively 1.294 and 0.122 eV, while the values were 1.464 and 0.003 eV for intermediate 3′ (Fig. 6). The nucleophilicity of ^{1}N was stronger than that of ^{2}N in both intermediates. Notably, the nucleophilicity of ^{1}N and ^{2}N in non-cyclic allenic 1,5-diamine intermediates 3 and 3′ remained unaffected when using (2-(but-3-en-1-yn-1-yl)phenyl)methanol 1 or hept-6-en-4-yn-1-ol 1′ as substrates.

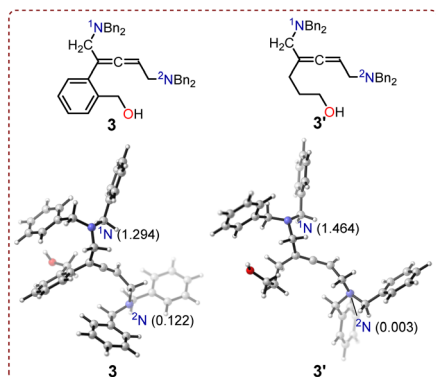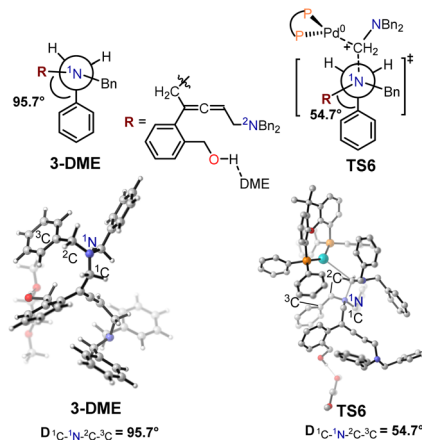Fig. 6 Calculated local nucleophilicity index N_k values.

Fig. 7 Structural information for intermediate 3-DME and transition state TS6.
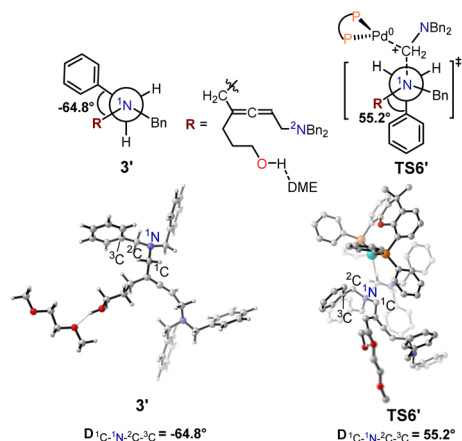
Fig. 8 Structural information for intermediate 3'-DME and transition state TS6'.
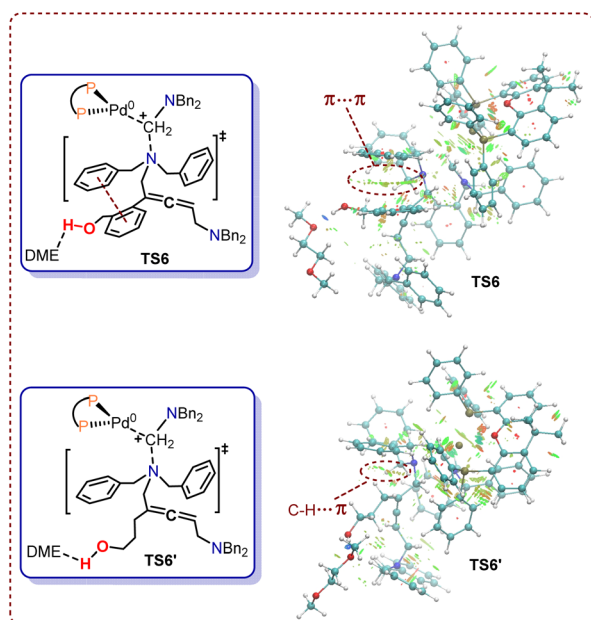

Fig. 9 Noncovalent interactions of TS6 and TS6' (blue, attraction; green, weak interaction; red, steric effect).

TS6'. This difference results in a lower distortion energy for **TS6** compared to **TS6'**, which consequently reduces the reactivity of the [1]N atom when the substrate is changed from (2-(but-3-en-1-yn-1-yl)phenyl)methanol **1** to hept-6-en-4-yn-1-ol **1′**.

Conclusions

In this work, DFT calculations were used to explore the mechanism of Huang's Pd-catalyzed cyclization reactions with an emphasis on the regioselectivity regulation mechanism. Theoretical calculations revealed that these reactions proceeded via migratory insertion, S_N2-type reductive elimination, and oxidative addition to give the non-cyclic allenic 1,5-diamine intermediate. The allenic amine and 1,3-diene O-heterocycle

products were then obtained through subsequent reductive elimination, S_N2-type substitution, and oxidative addition.

The reactivity of the [1]N atom decreased when (2-(but-3-en-1-yn-1-yl)phenyl)methanol instead of hept-6-en-4-yn-1-ol was used as the substrate, while the reactivity of the [2]N atom exhibited minimal change. This difference in reactivities of [1]N and [2]N contributed to the varying selectivity observed with different substrates. Distortion–interaction energy analysis and NCI calculations indicated that the presence of π–π stacking in intermediate **3-DME** led to the lower distortion energy of **TS6** than that of **TS6′**, consequently reducing the reactivity of the [1]N atom upon changing the substrate from (2-(but-3-en-1-yn-1-yl) phenyl)methanol to hept-6-en-4-yn-1-ol for regioselective control.

Data availability

The data that support the findings of this study have been included in the main text and ESI† and are available from the corresponding author upon reasonable request.

Author contributions

S. Liu conceived and designed the project. S. Liu designed the computational studies. D. Zhang, Y. Gong, L. Ma and L. Li performed the DFT calculations. S. Liu and W. Chen prepared the manuscript, D. Zhang, Y. Gong, L. Ma and L. Li prepared the ESI.†

Conflicts of interest

There are no conflicts to declare.

Acknowledgements

References

1 (a) S. Kaltenberger and M. V. Gemmeren, Controlling Reactivity and Selectivity in the Nondirected C–H Activation of Arenes with Palladium, *Acc. Chem. Res.*, 2023, **56**(18), 2459–2472; (b) K. Yamatsugu and M. Kanai, Catalytic Approaches to Chemo- and Site-Selective Transformation of Carbohydrates, *Chem. Rev.*, 2023, **123**(10), 6793–6838; (c) F. Juliá, Q. Shao, M. Duan, M. B. Plutschack, F. Berger, J. Mateos, C. Lu, X.-S. Xue, K. N. Houk and T. Ritter, High Site Selectivity in Electrophilic Aromatic Substitutions: Mechanism of C–H Thianthrenation, *J. Am. Chem. Soc.*, 2021, **143**(39), 16041–16054; (d) S. Bhadra and H. Yamamoto, Substrate Directed Asymmetric Reactions, *Chem. Rev.*, 2018, **118**, 3391–3446.

2 (a) L. Veth, H. A. Grab and P. Dydio, Recent Trends in Group 9 Catalyzed C–H Borylation Reactions: Different Strategies To Control Site-, Regio-, and Stereoselectivity, *Synthesis*, 2022, **54**, 3482–3498; (b) C. Nájera, I. P. Beletskaya and M. Yus, Metal-catalyzed regiodivergent organic reactions, *Chem. Soc. Rev.*, 2019, **48**, 4515–4618.

3 (a) J. F. Hartwig, Regioselectivity of the borylation of alkanes and arenes, *Chem. Soc. Rev.*, 2011, **40**, 1992–2002; (b) B. E. Haines, Y. Saito, Y. Segawa, K. Itami and D. G. Musaev, Flexible Reaction Pocket on Bulky Diphosphine–Ir Complex Controls Regioselectivity in para-Selective C–H Borylation of Arenes, *ACS Catal.*, 2016, **6**, 7536–7546; (c) K. Liao, T. C. Pickel, V. Boyarskikh, J. Bacsa, D. G. Musaev and H. M. L. Davies, *Nature*, 2017, **551**, 609–613; (d) M. Duan, C. D. Díaz-Oviedo, Y. Zhou, X. Chen, P. Yu, B. List, K. N. Houk and Y. Lan, Chiral Phosphoric Acid Catalyzed Conversion of Epoxides into Thiiranes: Mechanism, Stereochemical Model, and New Catalyst Design, *Angew. Chem., Int. Ed.*, 2022, **61**, e202113204.

4 (a) H. Chen, M. Farizyan and M. van Gemmeren, Regioselective Olefination of 3-Substituted Five-Membered Heteroarenes, *Eur. J. Org Chem.*, 2020, **40**, 6318–6327; (b) S. Negretti, A. R. H. Narayan, K. C. Chiou, P. M. Kells, J. L. Stachowski, D. A. Hansen, L. M. Podust, J. Montgomery and D. H. Sherman, Directing Group-Controlled Regioselectivity in an Enzymatic C–H Bond Oxygenation, *J. Am. Chem. Soc.*, 2014, **136**, 4901–4904; (c) J. M. Medina, J. L. Mackey, N. K. Garg and K. N. Houk, The Role of Aryne Distortions, Steric Effects, and Charges in Regioselectivities of Aryne Reactions, *J. Am. Chem. Soc.*, 2014, **136**, 15798–15805; (d) A. K. Hubbell and G. W. Coates, Nucleophilic Transformations of Lewis Acid-Activated Disubstituted Epoxides with Catalyst-Controlled Regioselectivity, *J. Org. Chem.*, 2020, **85**, 13391–13414.

5 (a) B. Zhou, T.-D. Tan, X.-Q. Zhu, M. Shang and L.-W. Ye, Reversal of Regioselectivity in Ynamide Chemistry, *ACS Catal.*, 2019, **9**, 6393–6406; (b) C. Sambiagio, D. Schönbauer, R. Blieck, T. Dao-Huy, G. Pototschnig, P. Schaaf, T. Wiesinger, M. F. Zia, J. Wencel-Delord, T. Besset, B. U. W. Maes and M. Schnürch, A comprehensive overview of directing groups applied in metal-catalysed C–H functionalisation chemistry, *Chem. Soc. Rev.*, 2018, **47**, 6603–6743; (c) Y. Xia and G. Dong, Temporary or removable directing groups enable activation of unstrained C–C bonds, *Nat. Rev. Chem*, 2020, **4**, 600–614; (d) G. Xia, J. Weng, L. Liu, P. Verma, Z. Li and J.-Q. Yu, Reversing conventional site-selectivity in C(sp³)–H bond activation, *Nat. Chem.*, 2019, **11**, 571–577; (e) T. Zhang, K. Zhong, Z.-K. Lin, L. Niu, Z.-Q. Li, R. Bai, K. M. Engle and Y. Lan, Revised Mechanism of C(sp³)–C(sp³) Reductive Elimination from Ni(II) with the Assistance of a Z-Type Metalloligand, *J. Am. Chem. Soc.*, 2023, **145**, 2207–2218.

6 (a) W.-T. Zhao, H. Meng, J.-N. Lin and W. Shu, Ligand-Controlled Nickel-Catalyzed Regiodivergent Cross-Electrophile Alkyl-Alkyl Couplings of Alkyl Halides, *Angew. Chem., Int. Ed.*, 2023, **62**, e202215779; (b) L. Zhao, Y. Zhu, M. Liu, L. Xie, J. Liang, H. Shi, X. Meng, Z. Chen, J. Han

and C. Wang, Ligand-Controlled NiH-Catalyzed Regiodivergent Chain-Walking Hydroalkylation of Alkenes, *Angew. Chem., Int. Ed.*, 2022, **61**, e202204716; (c) Q. Pan, Y. Ping, Y. Wang, Y. Guo and W. Kong, Ni-Catalyzed Ligand-Controlled Regiodivergent Reductive Dicarbofunctionalization of Alkenes, *J. Am. Chem. Soc.*, 2021, **143**, 10282–10291; (d) T. Xu, F. Sha and H. Alper, Highly Ligand-Controlled Regioselective Pd-Catalyzed Aminocarbonylation of Styrenes with Aminophenols, *J. Am. Chem. Soc.*, 2016, **138**, 6629–6635; (e) F. Schoenebeck and K. N. Houk, Ligand-Controlled Regioselectivity in Palladium-Catalyzed Cross Coupling Reactions, *J. Am. Chem. Soc.*, 2010, **132**, 2496–2497.

7 (a) H. J. Davis and R. J. Phipps, Harnessing non-covalent interactions to exert control over regioselectivity and site-selectivity in catalytic reactions, *Chem. Sci.*, 2017, **8**, 864–877; (b) F. O'Hara, D. G. Blackmond and P. S. Baran, Radical-Based Regioselective C–H Functionalization of Electron-Deficient Heteroarenes: Scope, Tunability, and Predictability, *J. Am. Chem. Soc.*, 2013, **135**, 12122–12134; (c) C. Schnepel and N. Sewald, Enzymatic Halogenation: A Timely Strategy for Regioselective C−H Activation, *Chem.– Eur. J.*, 2017, **23**, 12064–12086; (d) C. Wang, L. Luo and H. Yamamoto, Metal-Catalyzed Directed Regio- and Enantioselective Ring-Opening of Epoxides, *Acc. Chem. Res.*, 2016, **49**, 193–204.

8 (a) P.-S. Wang and L.-Z. Gong, Palladium-Catalyzed Asymmetric Allylic C–H Functionalization: Mechanism, Stereo- and Regioselectivities, and Synthetic Applications, *Acc. Chem. Res.*, 2020, **53**, 2841–2854; (b) H. Yue, C. Zhu, R. Kancherla, F. Liu and M. Rueping, Regioselective Hydroalkylation and Arylalkylation of Alkynes by Photoredox/Nickel Dual Catalysis: Application and Mechanism, *Angew. Chem., Int. Ed.*, 2020, **132**, 5787–5795; (c) S. Deng, C. Qu, Y. Jiao, W. Liu and F. Shi, Insights into 2-Indolylmethanol-Involved Cycloadditions: Origins of Regioselectivity and Enantioselectivity, *J. Org. Chem.*, 2020, **85**, 11641–11653; (d) B. Zhang, X. Xu, L. Tao, Z. Lin and W. Zhao, Rhodium-Catalyzed Regiodivergent Synthesis of Alkylboronates via Deoxygenative Hydroboration of Aryl Ketones: Mechanism and Origin of Selectivities, *ACS Catal.*, 2021, **11**, 9495–9505; (e) Q. Zhang, D. Dong and W. Zi, Palladium-Catalyzed Regio- and Enantioselective Hydrosulfonylation of 1,3-Dienes with Sulfinic Acids: Scope, Mechanism, and Origin of Selectivity, *J. Am. Chem. Soc.*, 2020, **142**, 15860–15869.

9 (a) H. Yu, B. Yu, H. Zhang and H. Huang, Palladium-Catalyzed Aminomethylation and Cyclization of Enynol to O-Heterocycle Confined 1,3-Dienes, *Org. Lett.*, 2021, **23**, 3891–3896; (b) B. Yu, M. Yu and H. Huang, Palladium-catalyzed ring-closing reaction of enynols with aminals via methylene transfer and C–N bond activation, *Tetrahedron Chem*, 2023, **7**, 100042.

10 M. J. Frisch, *Gaussian 16, Revision A.03*, Gaussian, Inc., Wallingford, CT, 2016. The full author list is given in the ESI.

11 (a) A. D. Becke, Density-functional thermochemistry. III. The role of exact exchange, *J. Chem. Phys.*, 1993, **98**, 5648–5652;

(*b*) C. Lee, W. Yang and R. G. Parr, Development of the Colle-Salvetticorrelation-energy formula into a functional of the electron density, *Phys. Rev. B: Condens. Matter Mater. Phys.*, 1988, **37**, 785–789; (*c*) H. L. Schmider and A. D. Becke, Optimized density functionals from the extended G2 test set, *J. Chem. Phys.*, 1998, **108**, 9624–9631; (*d*) K. Zhong, S. Liu, X. He, H. Ni, W. Lai, W. Gong, C. Shan, Z. Zhao, Y. Lan and R. Bai, Oxidative cyclopalladation triggers the hydroalkylation of alkynes, *Chin. Chem. Lett.*, 2023, **34**, 108339.

12 (*a*) M. Cossi, V. Barone, R. Cammi and J. Tomasi, Ab initio study of solvated molecules: a new implementation of the polarizable continuum model, *Chem. Phys. Lett.*, 1996, **255**, 327–335; (*b*) T. Liu, R. Duan, Y. Wang, S. Li, L. Qu, J. Song, Q. Liu and Y. Lan, Mechanistic investigation of zwitterionic MOF-catalyzed enyne annulation using UNLPF-14-MnIII as catalyst, *Chin. Chem. Lett.*, 2022, **33**, 4281–4286.

13 (*a*) Y. Zhao and D. G. Truhlar, A New Local Density Functional for Main-Group Thermochemistry, Transition Metal Bonding, Thermochemical Kinetics, and Noncovalent Interactions, *J. Chem. Phys.*, 2006, **125**, 194101; (*b*) Y. Zhao and D. G. Truhlar, The M06 Suite of Density Functionals for Main Group Thermochemistry,mThermochemical Kinetics, Noncovalent Interactions, Excited States, and Transition Elements: Two New Functionals and Systematic Testing of Four M06-Class Functionals and 12 Other Functionals, *Theor. Chem. Acc.*, 2008, **120**, 215–241; (*c*) Y. Zhao and D. G. Truhlar, Density Functionals with Broad Applicability in Chemistry, *Acc. Chem. Res.*, 2008, **41**, 157–167.

14 C. Y. Legault, *CYLView, 1.0b*, Université de Sherbrooke, Quebec, Canada, 2009, **https://www.cylview.org**, accessed 1 October 2017.

15 (*a*) F. Jensen, The magnitude of intramolecular basis set superposition error, *Chem. Phys. Lett.*, 1996, **261**, 633–636; (*b*) M. L. Senent and S. Wilson, Intramolecular basis set superposition errors, *Int. J. Quantum Chem.*, 2001, **82**, 282–292; (*c*) F. Jensen, Using valence bond methods to estimate intramolecular basis set superposition errors, *J. Chem. Phys.*, 2017, **146**, 184109; (*d*) F. Jensen, Basis Set Superposition Errors Are Partly Basis Set Imbalances, *J. Chem. Theory Comput.*, 2024, **20**, 767–774.

16 (*a*) E. R. Johnson, S. Keinan, P. Mori-Sánchez, J. Contreras-García, A. J. Cohen and W. Yang, Revealing Noncovalent Interactions, *J. Am. Chem. Soc.*, 2010, **132**, 6498–6506; (*b*) T. Lu and F. Chen, Multiwfn: A multifunctional wavefunction analyzer, *J. Comput. Chem.*, 2012, **33**, 580–592.

17 (*a*) L. R. Domingo, M. J. Aurell, P. Pérez and R. Contreras, Quantitative characterization of the global electrophilicity power of common diene/dienophile pairs Diels-Alder reactions, *Tetrahedron*, 2002, **58**, 4417–4423; (*b*) L. R. Domingo, E. Chamorro and P. Pérez, Understanding the Reactivity of Captodative Ethylenes in Polar Cycloaddition Reactions. A Theoretical Study, *J. Org. Chem.*, 2008, **73**, 4615–4624.

18 (*a*) L. R. Domingo and P. Pérez, The nucleophilicity N index in organic chemistry, *Org. Biomol. Chem.*, 2011, **9**, 7168–7175; (*b*) L. R. Domingo and P. Pérez, Global and local reactivity indices for electrophilic/nucleophilic free radicals, *Org. Biomol. Chem.*, 2013, **11**, 4350–4358.

19 P. K. Chattaraj, S. Duleya and L. R. Domingo, Understanding local electrophilicity/nucleophilicity activation through a single reactivity difference index, *Org. Biomol. Chem.*, 2012, **10**, 2855–2861.